Applied Thermal Engineering 303 (2026) 132141

Contents lists available at ScienceDirect

Applied Thermal Engineering

journal homepage: www.elsevier.com/locate/apthermeng

Research Paper

Knudsen pump for atmospheric and over-atmospheric pressure applications: System design, fabrication procedure and performance evaluation

Thanasis Basdanis [a], Phassawat Leelaburanathanakul [a], Thierry Camps [b], Marcos Rojas-Cárdenas [a], Christine Barrot [a], Lucien Baldas [a], Jürgen J. Brandner [c], Stéphane Colin [a,*]

[a] Univ Toulouse, IMT Mines Albi, INSA Toulouse, ISAE-SUPAERO, CNRS, ICA, Toulouse, France
[b] Univ Toulouse, CNRS, LAAS, Toulouse, France
[c] Institute of Microstructure Technology (IMT), Karlsruhe Institute of Technology, 76344 Eggenstein-Leopoldshafen, Germany

ARTICLE INFO

Keywords:
Microfluidics
Rarefied gas
Thermal creep
Micropump
Nanochannel

ABSTRACT

Knudsen pumps are promising candidates for vibration-free gas pumping in a variety of scientific and industrial applications, particularly where miniaturization is required. Based on thermal transpiration flows induced by temperature gradients along microchannels, they operate without moving parts and therefore offer high reliability. However, current fabrication techniques limit the realization of submicron channels needed for high performance operation at atmospheric and over-atmospheric pressures. To address this challenge, the present study investigates the feasibility of using Bessel beam technology for channel fabrication, enabling the creation of dense arrays of nanochannels with diameters of only a few nanometers at writing speeds of up to 1 kHz. Numerical simulations of gas flow and heat transfer were performed to design and optimize a single-stage, parallel-channel architecture while accounting for microfabrication constraints. The proposed design consists of 294,294 parallel nanochannels arranged within a 1×1 cm^2 glass substrate, each with a diameter of 600 nm and a length of 500 µm. Under simulated atmospheric operating conditions with moderate heating up to 100 °C, an average temperature difference of approximately 46.8 °C across the channels is predicted, resulting in a thermomolecular pressure difference of 1575 Pa and a maximum mass flow rate of 3.43×10^{-10} kg s^{-1}. When normalized by the total channel area, the predicted mass flow rate is much higher than that of previously reported Knudsen pumps, while maintaining a pressure difference among the highest values reported in the literature. The results demonstrate the potential of Bessel beam microfabrication for future high-performance Knudsen pumps operating at over-atmospheric pressures.

1. Introduction

Knudsen pumps have emerged as an attractive alternative to conventional gas pumping technologies in miniaturized systems due to their unique ability to transport gases, without any moving parts [1]. In recent years, they have been explored for a wide range of applications, including MEMS [2–4], hydrogen transfer [5,6], gas chromatography [7–9], aerosol sampling [10], heat pumps [11–13], space exploration instruments [14] and thrusters [15]. Their potential applications can also be extended to biomedical systems and sensors [16,17] as well as to the vibration-free operation of pulsed tube cryocoolers, enabling efficient cryogenic cooling for sensitive and microscopic systems [18–20]. Although some of these applications require compression above atmospheric pressures, Knudsen pumps have so far been investigated only under vacuum or atmospheric conditions, highlighting the need for further research into their operation at higher pressures. Addressing this gap is the focus of the present work.

Knudsen pumps are thermally driven flow pumps that operate on the

* Corresponding author.
E-mail addresses: basdanis@insa-toulouse.fr (T. Basdanis), leelabur@insa-toulouse.fr (P. Leelaburanathanakul), camps@laas.fr (T. Camps), rojascar@insa-toulouse.fr (M. Rojas-Cárdenas), lattes@insa-toulouse.fr (C. Barrot), baldas@insa-toulouse.fr (L. Baldas), juergen.brandner@kit.edu (J.J. Brandner), stephane.colin@insa-toulouse.fr (S. Colin).

https://doi.org/10.1016/j.applthermaleng.2026.132141
Received 8 April 2026; Received in revised form 4 June 2026; Accepted 24 June 2026
Available online 1 July 2026
1359-4311/

basis of transpiration flow [21–25], a phenomenon that occurs under rarefied conditions when the channel dimensions are comparable to the mean free path of the gas molecules. By applying temperature gradients along micro- or nanochannels, a gas movement is created from cold to hot areas. Thermal transpiration has been investigated extensively in numerical works [26–30], while experimental results are scarcer [31–34]. Eliminating the need for moving parts, Knudsen pumps provide simplicity, reliability, and long lifetime [1,35], while their small size makes them ideal for miniaturized systems [36]. Although the generated mass flow rates are relatively small compared with conventional macroscopic pumps, they can become significant for microscale systems and applications requiring compact, vibration-free, and highly reliable gas transport under atmospheric-pressure conditions.

Different design approaches have been explored, ranging from porous media [37–40] to lithographically microfabricated channels [4,9,35,41]. Although porous media may be more suitable to reach the required rarefied conditions for Knudsen pump applications, natural defects often appear, which can restrict gas flow and reduce efficiency. In addition, their geometrical features are often poorly characterized, which complicates simulation and optimization. In contrast, fabricating microchannels may be a more effective option since they enable more efficient designs, drastically reduce geometrical uncertainties and thus offer better control in terms of gas flow regulation [35]. Tapered channels can further enhance the pressure head, though at the expense of mass flow rate [42,43]. To date, efforts to enhance the relatively low performance of Knudsen pumps have primarily focused on either increasing the pressure head —by pumping air from atmospheric pressure down to 0.46 atm [4]— or increasing the mass flow rate, reaching 8.8×10^{-10} kg s^{-1} through a 10^{-3} mm^2 channel opening [35]. Designs incorporating multiple parallel channels to enhance mass flow rate and multiple stages in series to increase the pressure head have also been proposed [9,40,44]. These ongoing efforts highlight the potential for performance improvements and pave the way for investigating operation over atmospheric pressures.

The degree of rarefaction is determined by both the pressure and the characteristic length scale of the channels. As a result, the optimal channel dimensions for thermal transpiration applications strongly depend on the intended working pressure. For vacuum applications, the optimal characteristic length ranges from several microns to tens of microns, depending on the working pressure and the gas, making it feasible to fabricate the channels with existing fabrication technologies [35,45–49]. One of the most widely applied recent methods for fabricating channels in Knudsen pumps is deep reaction ion etching (DRIE), which allows the production of channels with dimensions as small as some microns [9,35,41]. However, DRIE is typically limited to relatively small aspect ratios, i.e., the length-to-diameter ratio does not typically exceed 20, and channel dimensions are on the order of 1 μm. These limitations can make the fabrication of Knudsen pumps intended for atmospheric or over-atmospheric operation more challenging, since submicron characteristic dimensions are preferred to reach the optimal rarefaction conditions.

To overcome these limitations, the present work proposes the use of Bessel beam technology for nanochannel fabrication [50,51]. In this approach, narrowly focused laser pulses are absorbed within transparent materials such as glass, generating localized heating and material sublimation that enable the formation of vertically oriented through-substrate nanochannels. In contrast to DRIE, Bessel beam processing can produce channels with diameters below 200 nm and aspect ratios exceeding 100, while also allowing the channel diameter to be tuned through adjustment of the laser pulse energy. In addition, the technology offers extremely high writing speeds [52] making it particularly promising for the fabrication of dense nanochannel arrays required for atmospheric-pressure Knudsen pumps. Nevertheless, limitations still exist regarding channel spacing, since a minimum separation distance of approximately 10 μm is currently required to reduce the risk of crack formation and substrate damage during fabrication.

In the present work, we propose a novel design along with a numerical analysis of heat and mass transport for a Knudsen pump intended to operate from atmospheric to higher pressures. The design incorporates advanced microfabrication techniques aimed at extending current fabrication limits for nanochannel manufacturing and optimized thermal architecture. The originality of the study lies primarily in the use of advanced Bessel beam microfabrication technology for nanochannel fabrication, while the heat transfer and gas flow modeling are based on well-established ANSYS Mechanical simulations and kinetic theory, respectively, which are applied here to optimize the pump design and assess its performance. This study is part of a collaborative project between INSA Toulouse and the Karlsruhe Institute of Technology (KIT), conducted within the framework of the PuCK project, which focuses on the development and integration of a Knudsen pump prototype and a miniaturized pulse tube cryocooler system, enabling vibration-free cryogenic cooling.

In order to achieve the mass flow rates and pressure differences required for demanding applications such as the miniaturized pulse tube cryocooler (PTCC) targeted within the PuCK project, i.e., a mass flow rate of 10^{-7} kg s^{-1} and a pressure difference of 1 bar, Knudsen pumps incorporating multiple parallel channels and stages in series must be designed [53]. These requirements are particularly challenging because both high mass flow rates and significant compression must be achieved simultaneously under atmospheric-pressure conditions. In contrast, other Knudsen-pump applications primarily requiring high flow rates with negligible pressure differences and low operating pressures may allow the use of larger channel dimensions and more conventional fabrication techniques. Consequently, channel dimensions must be optimized based on the rarefaction conditions that enhance the performance of the Knudsen pump under the working pressures, while thermal management strategies should be refined to maximize temperature gradients along the channels. These design improvements should be examined within the limitations set by the fabrication techniques currently available, ensuring the feasibility and functionality of the proposed design.

The paper is structured as follows. Section 2 presents the pump design; Section 3 describes the gas flow simulations used to determine the channel dimensions; Section 4 discusses the heat transfer simulations and the optimal design of heaters and heat sink; Section 5 details the fabrication process of the one-stage Knudsen pump; Section 6 focuses on the kinetic modeling of pumps with multiple parallel channels and stages; and Section 7 concludes the paper.

2. Design

The proposed Knudsen pump has been designed to maximize the mass flow rate and pressure difference within a 2×2 cm^2 footprint, using the Bessel beam technology for fabrication of the nanochannels, while ensuring effective thermal management and structural stability. Fig. 1 provides a 3D CAD model of the Knudsen pump which corresponds to a system composed of the glass plate with the nanochannels, the silicon-based heat sink with micro-pillars, and the integrated heaters. Fig. 2 provides a detailed top view of a small central area of the Knudsen pump, showing the heaters, nanochannels, and silicon pillars in greater detail. Although the heaters are located on the top side and the silicon pillars on the bottom side of the glass, both are represented on the same plane.

A four-inch-diameter glass wafer with a thickness $t_g = 500\,\mu$m is used and divided into nine square sections, each with a side length $a = 2$ cm and functioning as an individual pump (Figs. 1a–c). Within each 2×2 cm^2 glass piece, the central square region, with a side length $b = 1$ cm, is occupied by nanochannels with a diameter $d_c = 600$ nm, etched through the entire glass thickness and arranged in a hexagonal pattern to maximize packing efficiency while maintaining a spacing $l_c = 20\,\mu$m.

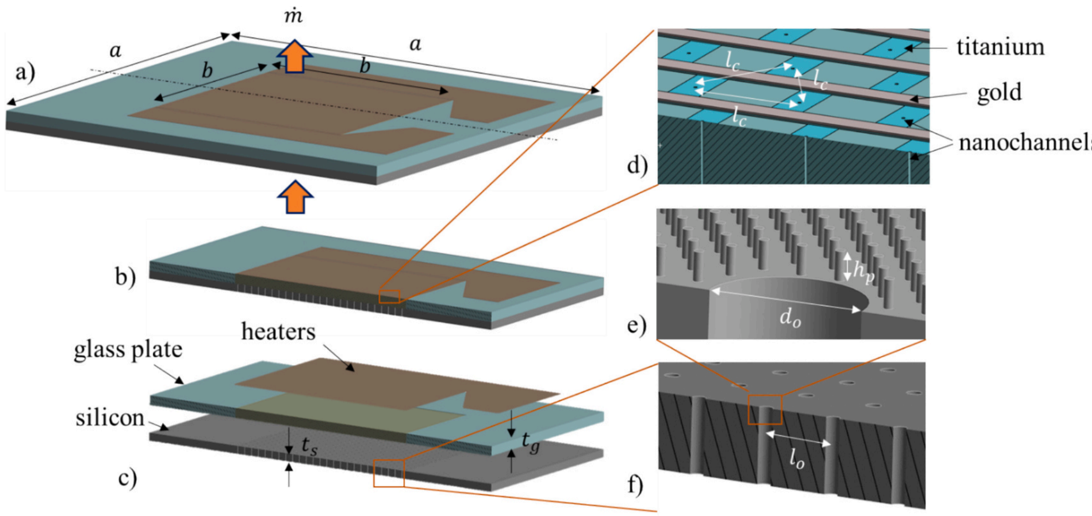

Fig. 1. Single stage Knudsen pump: a) complete design, b) half-section view, c) half-section exploded view with heaters, glass plate and silicon heat sink layers, d) magnified view of the heaters and nanochannels, e) magnified view of the silicon pillars and f) magnified view of the silicon wafer with 80 μm-diameter openings.

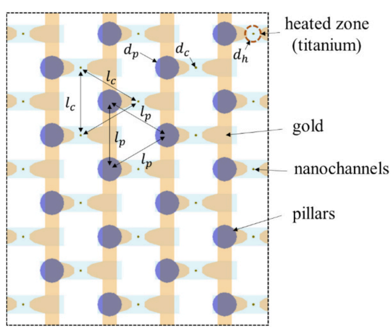

Fig. 2. Detailed top view of a central area of the Knudsen pump, showing the heaters (heated zone), nanochannels, and pillars.

This configuration results in a total of 294,294 channels (Figs. 1d and 2). The remaining area is reserved for heater and heat-sink connections.

To establish and sustain a temperature gradient across the glass thickness, thin-film heaters are deposited on the top surface of the glass, while a silicon-based heat sink is bonded to the opposite side (Fig. 1c). The heaters consist of two successive metal layers: a titanium film with a thickness of 20 nm in contact with the glass, and a gold layer with a thickness of 300 nm deposited on top (Figs. 1d and 2). Although the geometry of the gold layers is simplified in the 3D representation of Fig. 1, their actual shape, including the rounded edges, is shown in the detailed view of Fig. 2. The gold layer serves as a conductive track for electronic wiring with negligible Joule dissipation, whereas the thinner titanium regions are responsible for generating the localized heating around each channel, indicated by the heated zones shown in light blue in Fig. 2. The ends of the gold pads are designed with a rounded geometry, which leads to a higher concentration of current density and Joule heating near the center of the titanium region compared with its lateral sides. As a result, the effective heating region around each nanochannel can be reasonably approximated by a circular heated zone, with a diameter $d_h = 6\ \mu$m. For the heat-transfer simulations, equivalent circular heating areas centered around the channels were therefore used. On the underside, silicon pillars with a diameter $d_p = 7\ \mu$m and a height $h_p = 15\ \mu$m are fabricated on top of a silicon wafer with a thickness $t_s = 400\ \mu$m (Fig. 1c and e), which is bonded to the glass. The pillars are arranged in a hexagonal pattern with a spacing $l_p = l_c = 20\ \mu$m and are offset by 8.5 μm from the channel positions, ensuring efficient heat removal from the cold side of the glass while limiting pressure drop in the gas flow. In addition, openings with a diameter $d_o = 80\ \mu$m are etched through the full thickness of the silicon wafer at a spacing $l_o = 400\ \mu$m, allowing gas to pass from the underside (Fig. 1f).

The combined heater–heat sink arrangement is designed to enhance the thermal efficiency of the Knudsen pump, enabling localized heating near every channel while rapidly dissipating heat from the cold side. The placement of heaters and heat sinks around the channels ensures that temperature gradients are sharply defined, a key factor for the performance of the pump. The following sections provide a detailed explanation of the system architecture based on gas flow and heat transfer modeling, as well as the fabrication steps.

3. Gas flow modeling

To optimize the pump architecture for over-atmospheric pressure conditions, modeling via kinetic theory of a thermal transpiration flow through one circular channel is considered. Owing to the large length-to-radius ratio of the channel, the mass flow rate $\dot{m}$ and the pressure distribution $P(z)$ along the capillary axis ($z \in [0, l]$) are computed according to the infinite capillary theory as [54,55]:

$$\frac{dP}{dz} = -\frac{v_0(z)}{\pi R^3\ G_P(\delta)}\dot{m} + \frac{P(z)}{T(z)}\frac{G_T(\delta)}{G_P(\delta)}\frac{dT}{dz} \tag{1}$$

where $v_0(z) = \sqrt{2R_g\ T(z)}$ is the most probable speed of the gas molecules, $R_g = k_B/m$ is the specific gas constant, k_B is the Boltzmann constant, m is the molecular mass, R is the radius of the channel, $T(z)$ is the temperature distribution and G_P and G_T are the dimensionless kinetic flow rates for the Poiseuille and thermal creep flows, respectively. These flow rates are obtained from the linearized Shakhov kinetic model assuming purely diffuse boundary conditions, and can be found in the supplementary material of [56]. The flow rates are given as a function of the gas rarefaction parameter $\delta(z)$ defined as:

$$\delta(z) = \frac{P(z)\ R}{\mu(z)\ v_0(z)} \tag{2}$$

where $\mu(z) = \mu(T_{ref})\left[T(z)/T_{ref}\right]^{\omega}$ is the viscosity computed based on the reference viscosity at a reference temperature T_{ref} and the viscosity exponent ω. Once the geometrical and gas characteristics are provided, Eq. (1) can be numerically solved for a given temperature distribution $T(z)$, to either compute the mass flow rate $\dot{m}$ when the inlet and outlet pressures are known, or to compute the outlet pressure P_{out} when the mass flow rate $\dot{m}$ and the inlet pressure P_{in} are known. In the case of zero mass flow rate, the maximum pressure difference, also known as thermomolecular pressure difference (TPD), can be obtained, while, when the inlet and outlet pressures are set equal to each other, the maximum mass flow rate which corresponds to the thermal creep flow can be computed. During the numerical resolution of Eq. (1), the local rarefaction parameter $\delta(z)$ and the corresponding kinetic coefficients $G_P(\delta)$ and $G_T(\delta)$ are continuously updated at each position z according to the local pressure and temperature conditions, following the procedure described in [55]. Intermediate cases can also be computed to obtain the characteristic curve of the Knudsen pump [53,55]. The numerical code developed to solve Eq. (1) was validated against previous numerical and experimental studies. Fig. 3a compares the present results with the experimental data reported in [57] for thermal creep flow of helium, argon and nitrogen through a long tube of diameter $d = 485\ \mu$m, length $l = 52.7$ mm, subjected to a temperature difference of 71 K. In this figure, the TPD, $\Delta P_{\max}$, is plotted as a function of the mean rarefaction parameter δ_m defined at the mean pressure and temperature conditions. Fig. 3b presents a comparison with the numerical study of [58] for hard sphere argon flowing in a tube of diameter $d = 0.3\ \mu$m, length $l = 500\ \mu$m and a temperature ratio $T_{out}/T_{in} = 293/77.2 = 3.8$, and the numerical study of [58] for the same gas but with a diameter $d = 0.4\ \mu$m, a length $l = 500\ \mu$m and a temperature ratio $T_{out}/T_{in} = 600/300 = 2$. The maximum mass flow rate, $\dot{m}_{\max}$, obtained for $\Delta P = 0$, is plotted as a function of the inlet rarefaction parameter δ_{in} calculated based on the inlet pressure and temperature. In the first case, the present numerical results reproduce the experimental measurements within the range of deviations previously reported in the literature [29,34,59]. In case of the numerical results, an excellent agreement is observed with a divergence of less than 1% between the results.

In the present study, the pump performance is evaluated in terms of mass flow rate. While the volumetric flow rate therefore varies along the channel, the mass flow rate remains conserved and provides a more fundamental measure of the pump performance. For Knudsen pumps which operate under rarefied conditions, the primary objective is not to improve the energetic efficiency, but rather the generation of pressure differences and controlled gas transport without moving parts. Therefore, the optimization of the pump focuses mainly on identifying the rarefaction conditions that maximize the attainable mass flow rate and pressure difference under the targeted operating conditions [35].

To specify the optimal radius for the channels, the rarefaction regime under which the Knudsen pump will work should be specified. In Fig. 4, the maximum pressure difference and the maximum mass flow rate are plotted in terms of the mean pressure $P_m = (P_{in} + P_{out})/2$. These results are obtained by solving Eq. (1) for a linear temperature distribution along the channel, $T(z) = T_{in} + (T_{out} - T_{in})z/L$, where the inlet and outlet temperatures are $T_{in} = 323$ K and $T_{out} = 373$ K, respectively. These indicative temperatures are consistent with the heat transfer simulations reported in Section 4. The channel length is set to $l = 500\ \mu$m and the working gas is nitrogen. Nitrogen was used as the working gas throughout the present work, as its properties provide a good approximation of atmospheric air. The results are provided for three different values of radius $R = [0.2, 0.3, 0.4]\mu$m chosen such that the optimum TPD, $\Delta P_{\max}$ (for $\dot{m} = 0$), occurs near atmospheric pressure. For $R = 0.3\ \mu$m, the optimum value of $\Delta P_{\max}$ coincides with a mean pressure $P_m = 1$ atm; for $R = 0.2\ \mu$m, the optimum occurs at slightly higher pressure, while for $R = 0.4\ \mu$m, it occurs at slightly lower pressure. In contrast, the maximum mass flow rate $\dot{m}_{\max}$ (for $\Delta P = 0$) increases monotonically with P_m, although the rate of increase gradually diminishes at higher pressures, exhibiting an inflection point. It is also noted that, for a fixed operating pressure, $\dot{m}_{\max}$ increases monotonically with the channel radius, since larger radii correspond to higher values of the rarefaction parameter δ. As shown in Fig. 3b, $\dot{m}_{\max}$ continuously increases with increasing δ. Consequently, unlike the thermomolecular pressure difference, no optimum radius maximizing the mass flow rate is observed. Therefore, for the present work, the Knudsen pump is designed with a radius of $R = 0.3\ \mu$m which maximizes $\Delta P_{\max}$ while providing a reasonable $\dot{m}_{\max}$. All these characteristics are accounted for in the pump design, in conjunction with the heat transfer results.

By solving Eq. (1) for intermediate values of the mass flow rate $\dot{m} \in [0, \dot{m}_{\max}]$, the characteristic curve of the Knudsen pump is obtained and is plotted in Fig. 5 for three different radius values $R = [0.2, 0.3, 0.4]\mu$m. As it is expected from the results of Fig. 4, $\Delta P_{\max}$ increases and $\dot{m}_{\max}$ decreases as the radius decreases. It is also observed that the characteristic curve for a single channel is linear between the two limit points $[\dot{m} = 0, \Delta P_{\max}]$ and $[\dot{m}_{\max}, \Delta P = 0]$.

To meet the requirements of potential applications, the flow characteristics of a single channel are insufficient, since much higher mass flow rates and pressure differences are usually needed. Therefore, multiple channels should be arranged in parallel to increase the mass flow rate, while multiple stages should be stacked in series to enhance the pressure difference. The performance study of the pump with the 294,294 parallel channels is given in Section 6, based on the heat transfer results from Section 4.

4. Heat transfer modeling

To optimize the temperature gradient across the glass thickness, i.e., along the channel length, heat transfer simulations were performed to improve the thermal architecture of the system, including the positioning and dimensions of the heaters and heat sink, as well as the selection of suitable materials. In thermal transpiration flow, greater temperature differences result in higher pressure differences ΔP and mass flow rates $\dot{m}$. From a heat transfer perspective, Fourier's law states that for the same heat flux, materials with lower thermal conductivity

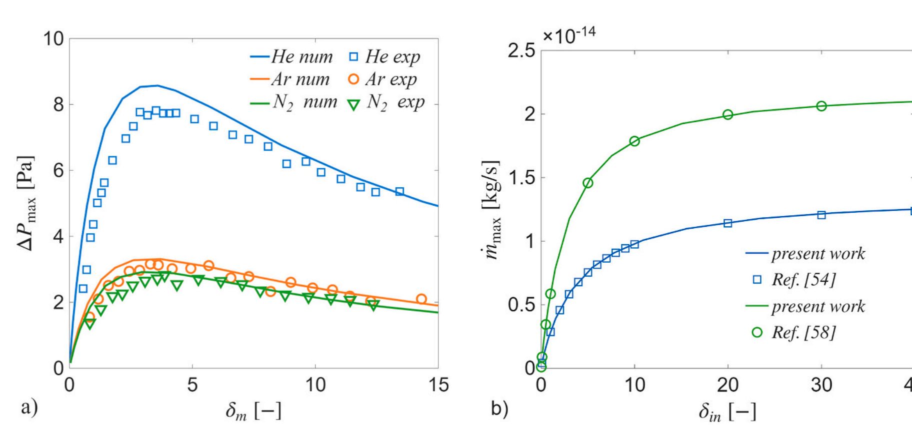

Fig. 3. Validation of the present numerical model for thermal creep flow: a) comparison with the experimental data reported in [57]; b) comparison with the numerical results reported in [54,58].

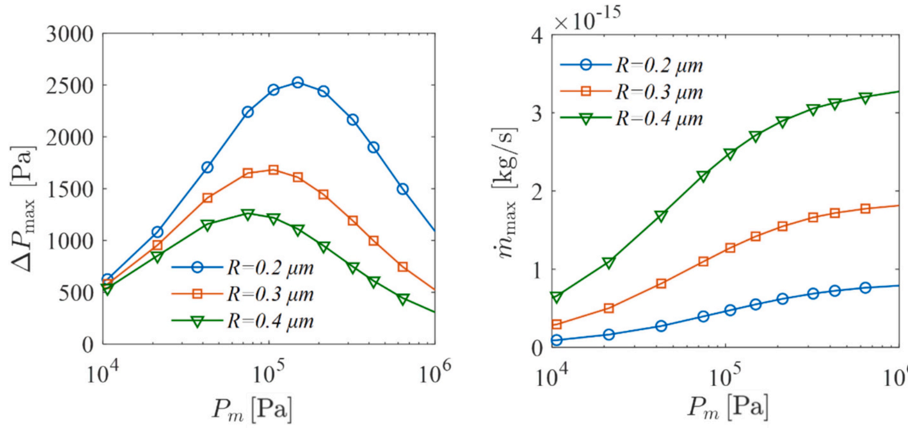

Fig. 4. Maximum pressure difference (left), and maximum mass flow rate (right) vs mean pressure.

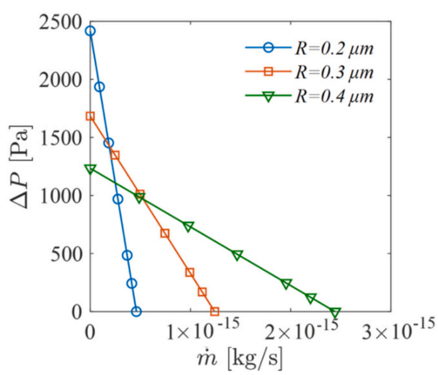

Fig. 5. Pressure difference vs mass flow rate for three radius values $R = [0.2, 0.3, 0.4] \mu m$.

create larger temperature gradients. Thus, the low thermal conductivity k of glass, around 1 W m^{-1} K^{-1}, justifies the choice of using a glass plate for the fabrication of the channels. To achieve a temperature gradient across the glass thickness, heaters were applied to the top hot-side of the device (Fig. 1). However, natural convection alone is often insufficient for rapid heat dissipation on the opposite cold-side, and thus, it was proposed to add a heat sink on this side to enhance cooling. From a material standpoint, the heaters should have high thermal conductivity to distribute heat efficiently while also exhibiting moderate electrical resistivity to distribute efficiently the electric charge and generate heat locally when power is applied. For this reason, thin metal deposition layers such as platinum, gold, or titanium are commonly used [60–62]. In this study, gold and titanium layers with electrical resistivity ρ at 373 K of 3.1×10^{-8} Ω m and 5.48×10^{-7} Ω m, respectively, are applied, with their thickness and sequence determined by fabrication techniques and adhesion requirements. Further details on fabrication are provided in the next section. For the heat sink, materials with high thermal conductivity are necessary to rapidly dissipate heat from the cold side of the glass plate, maintaining a low temperature [63,64]. Thus, silicon was selected due to its high thermal conductivity $k = 150$ W m^{-1} K^{-1}, compatibility with glass for bonding purposes, ease of fabrication, and structural properties. In this work, various heat source and heat sink coupling designs have been tested, ranging from simpler, easier-to-fabricate but less efficient solutions (without heat sinks) to more advanced configurations (with heat sinks and optimized designs), while always complying with the constraints imposed by the fabrication processes. These investigations led to the design presented in Section 2.

In an initial design approach without a heat sink, two linear heaters, each 5 μm wide and 1 cm long, were deposited on the 1×1 cm^2 hot-side of the glass plate to establish a temperature gradient along the channels, while heat dissipation on the opposite side relied solely on natural convection. The channels were positioned close to the heaters in an area extended until the temperature gradient became negligible. Increasing the number of linear heaters resulted in a decrease in the average temperature difference ΔT across the channels, even though more channels could be integrated. Thus, natural convection alone was insufficient to effectively cool the cold side of the plate, making it difficult to achieve significant temperature gradients through the glass thickness. Only a limited area of the 1×1 cm^2 hot-side of the glass plate could be covered with heaters and channels, leading to negligible gradients across the channels as their number increased. Fig. 6 presents the average temperature difference ΔT across the channels as a function of the number of channels, showing that increasing this number decreases ΔT due to inefficient cooling on the opposite side. Additional simulations investigating alternative heater configurations, such as circular heaters surrounded by channels, produced similar results. Therefore, incorporating a heat sink was found to be essential to achieve larger temperature differences across the channels.

The placement of heaters and heat sinks close to each channel creates sharp temperature gradients, which in turn maximize the mass flow rate and pressure difference of the pump. This is more pronounced when both heaters and heat sinks are integrated around every channel within the 1×1 cm^2 active area of the glass plate, leading to the design presented in Fig. 1.

A single three-dimensional heat-transfer simulation of the complete Knudsen pump was conducted in ANSYS Mechanical under steady-state conditions. The mesh created for the simulation is presented in Fig. 7 while the temperature profiles are presented in Fig. 8. The full 2×2 cm^2 footprint of the Knudsen pump was included in the computational

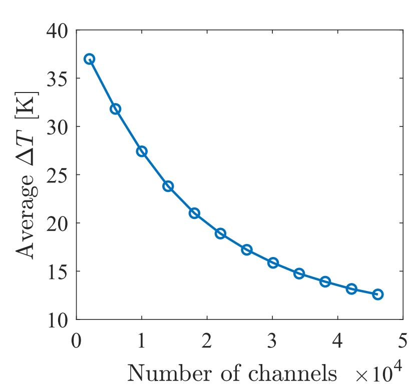

Fig. 6. Average temperature difference across the channels as a function of the number of channels for the no-heat-sink configuration.

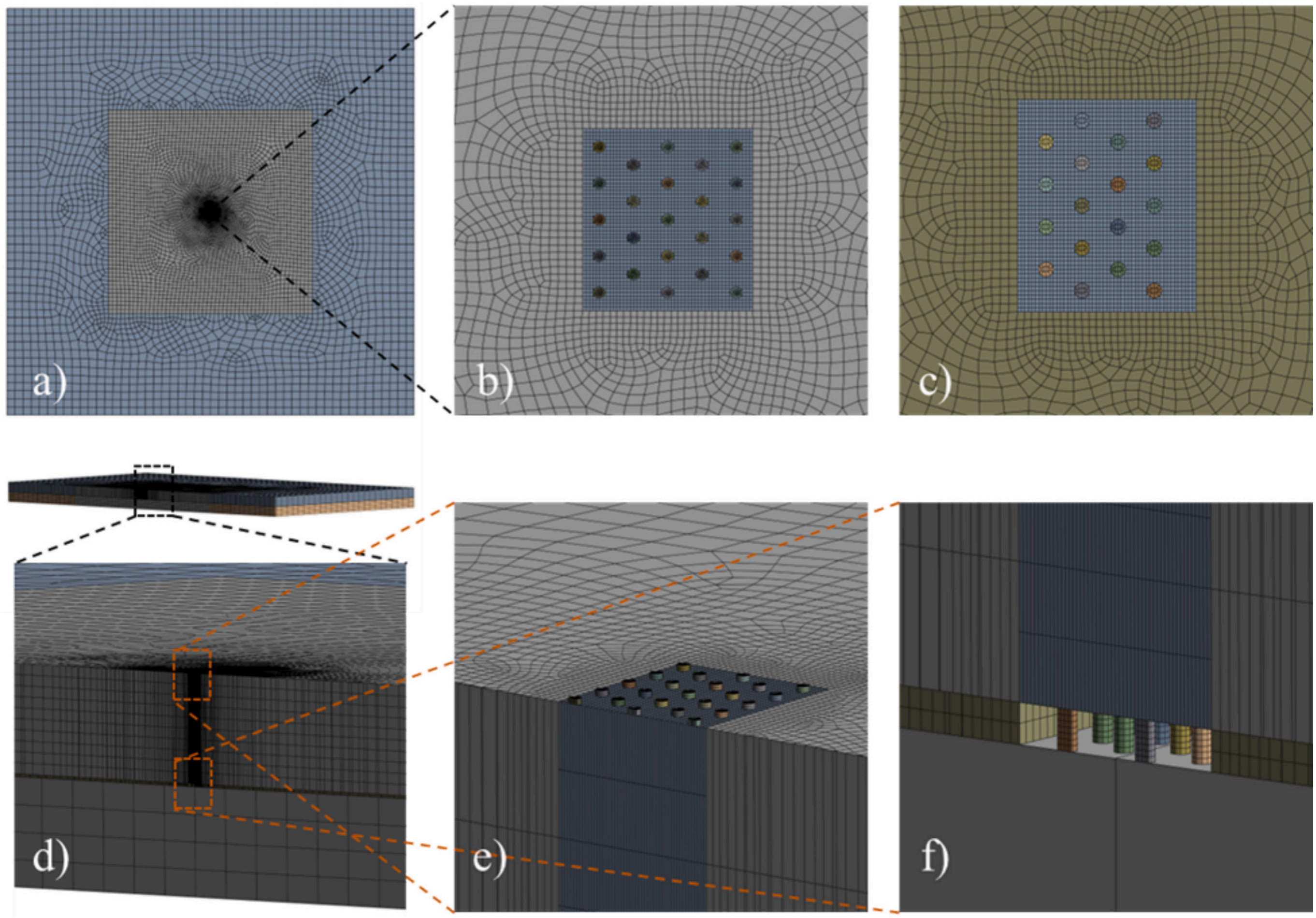

Fig. 7. Mesh generated in ANSYS Mechanical for the heat transfer simulation: a) top view of the complete design, b) detailed top view of the small central area, c) detailed view of glass bottom including the pillars, d) half-section view of the complete design including a detailed view in the center, e) detailed view of the heaters and surrounding area, and f) detailed view of the pillars and surrounding area.

domain in order to capture the global temperature distribution across the glass plate. In addition, a locally refined central region shown in Fig. 7 was explicitly modeled with higher mesh resolution to resolve the detailed temperature gradients generated by the individual heaters and silicon pillars. The finite element mesh consists of approximately one million nodes, leading to a resolution that ensured mesh-independent results. Therefore, the global temperature distributions shown in Figs. 8a–b and the detailed local temperature distributions shown in Figs. 8d–e originate from the same simulation. The inclusion of the full pump geometry was necessary to capture large-scale heat spreading and edge-cooling effects, which cannot be resolved using only the locally refined region.

For the simulation, each component has been assigned appropriate thermal properties, which are summarized in Table 1 together with their geometric characteristics. The modeling assumptions and simplifications are summarized as follows:

a) A locally refined mesh was applied within a small central region of the glass plate corresponding to the top view geometry shown in Fig. 2, where the individual heaters and silicon pillars were explicitly resolved in order to capture the local temperature nonuniformities shown in Fig. 8d and e. In Fig. 8d, the red circular regions correspond to the equivalent localized heating zones associated with the titanium heaters surrounding each nanochannel. Although the actual titanium tracks are not circular, the rounded ends of the gold traces concentrate the current density and Joule heating near the center of the heater geometry. Therefore, equivalent circular heating regions were used in the simulations to accurately reproduce the resulting local temperature gradients around the nanochannels. In Fig. 8e, the blue circular regions correspond to the silicon pillars located beneath the glass plate, which locally enhance heat extraction and therefore reduce the temperature near the pillar contacts.

b) A total heating power of 10 W was applied. Specifically, a uniform heat flux $q = 10^5$ W m^{-2} was imposed on the 1×1 cm^2 active area on the top surface of the glass (outside the central detailed model), while a higher heat flux $q_{heaters} = 12 \times 10^5$ W m^{-2} was applied to the top surfaces of the heaters. This value was calculated based on the area that is covered by the heaters as $q_{heaters} = qA_{uniform}/A_{heaters}$ where $A_{uniform}$ and $A_{heaters}$ correspond to the 1×1 cm^2 active area and the area covered by the 294,294 heaters, respectively.

c) An equivalent thermal conductivity equal to $k_{eq} = 17$ W m^{-1} K^{-1} was assigned to the silicon heat sink with the pillars to account for the area fraction they occupy, calculated as $k_{eq} = k_{silicon}A_{pillars}/A_{uniform}$, where $k_{silicon}$ is the thermal conductivity of silicon and $A_{pillars}$ is the area covered by the 294,294 pillars. In this estimation, the thermal conductivity of air was considered negligible compared with that of silicon. Outside the locally refined region, the dense pillar array was therefore represented using this equivalent thermal conductivity approach in order to reduce the computational cost while preserving the correct average heat-transfer behavior across the full pump area.

d) The 80 µm-diameter through-openings of the silicon wafer were not explicitly included in the present heat-transfer simulation in order to

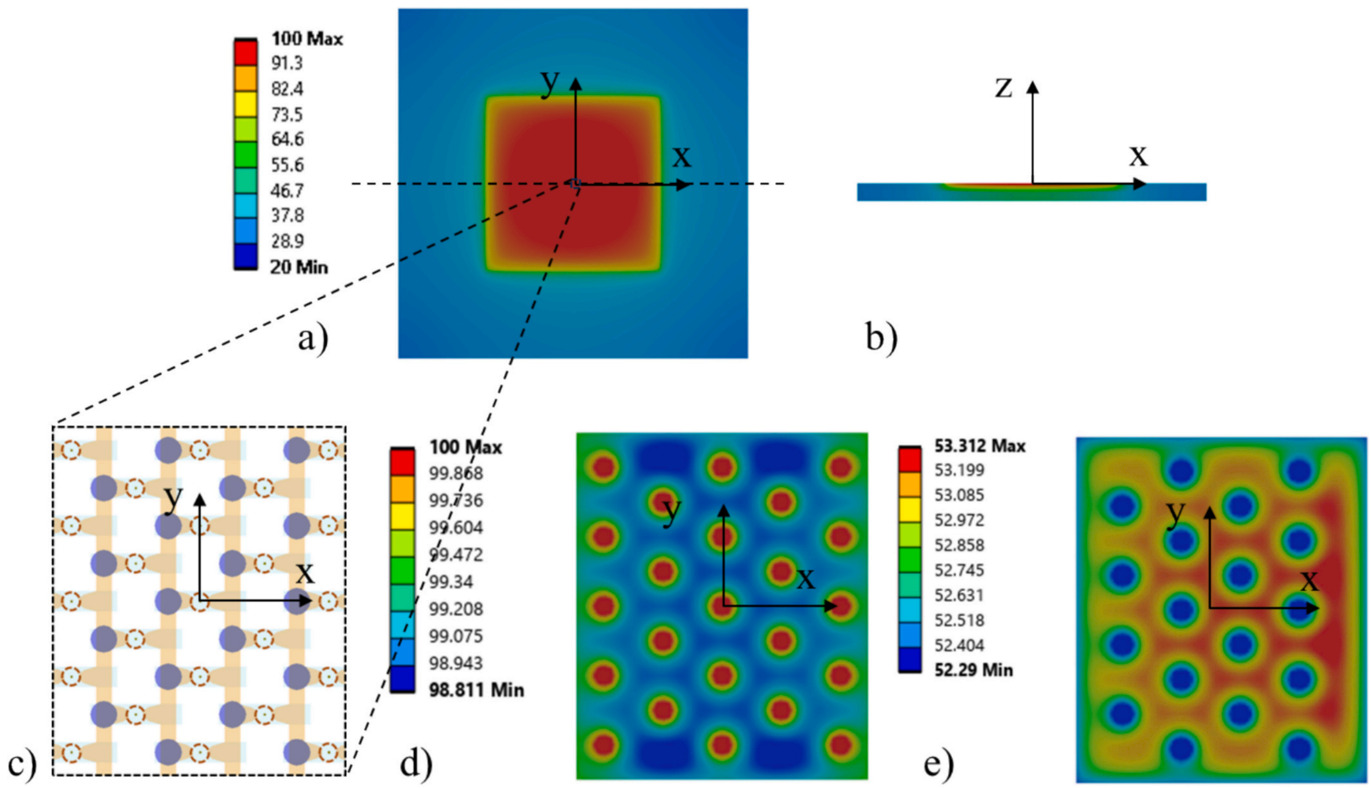

Fig. 8. Temperature distributions (in °C) simulated within a single-stage Knudsen pump: a) top view of complete design, b) cross-sectional view of full design, c) detailed top view of a central area of the design, d) detailed view of glass top beneath the heaters, f) detailed view of glass bottom above the pillars.

Table 1
Materials, properties and geometric characteristics for the thermal simulation.

Material	Thermal conductivity [W m^{-1} K^{-1}]	Top view area [mm^2]	Thickness/ height [μm]
Borosilicate glass	1	20×20	500
Silicon plate	150	20×20	400
Silicon pillars	150	$\pi \cdot 0.0035^2$	15
Equivalent for silicon with pillars	17	10×10	15
gold	314		0.3
titanium	11		0.02

reduce the geometrical complexity of the computational model. Nevertheless, their thermal influence is expected to remain limited, since the area occupied by the openings corresponds to only approximately 3.14% of the active area, while their diameter remains significantly smaller than the 500 µm glass thickness, promoting lateral heat spreading within the glass. Consequently, no significant influence on the average temperature difference across the nanochannels, and therefore on the predicted gas-flow performance, is expected.

e) The Knudsen pump was exposed to ambient air at 20 °C on its top and surrounding surfaces. Therefore, natural convection was applied to account for heat dissipation, while thermal radiation was evaluated and found to have a negligible effect. On the bottom side, outside the 1×1 cm^2 active area, an efficient heat sink capable of extracting 10 W of heat was considered. For the simulation, the metallic support planned for the future experimental testing of the pump was modeled, assuming that regions sufficiently far from the pump were maintained at 20 °C. However, several types of heat sink have been proposed in the literature capable of extracting the amount of 10 W through a 3 cm^2 area. Among them, microchannel heat sinks have emerged as one of the most effective thermal management solutions, offering a large specific surface area, small size, reduced coolant demand, and high heat transfer coefficient [65–68]. Alternatively, extended-surface configurations such as pin-fin heat sinks have been investigated to enhance natural or forced convection [69–71]. Other approaches include biporous metal foam heat sinks [72] and hybrid designs that integrate high-conductivity fins with phase change materials (PCMs) [73]. The selection of a suitable heat sink depends on the intended application of the Knudsen pump, as different operational environments impose different requirements on thermal management strategies. In some cases, heat sinks may not be necessary if the Knudsen pump is installed on a device that can provide adequate heat dissipation.

The average temperature difference across the 294,294 channels was found to be 46.8 K, indicating a significant improvement compared to simpler designs. Temperature contours of the top and bottom surfaces of the glass plate are also provided, showing a relatively uniform temperature distribution on both sides. Therefore, the current size and spacing of the heaters and silicon pillars effectively heat the top surface and cool the bottom surface of the glass, while also allowing room for additional channels that could be incorporated based on future fabrication improvements, without the need for extra heaters or pillars. It was also observed that the temperature gradients along the 294,294 channels changes depending on the position of the channel. Even for a uniform heat flux over the 1×1 cm^2 area, the temperature difference between the top and bottom surfaces of the glass varies due to the different rates of heat dissipation at different locations. Fig. 9 shows the temperature distributions along the central line x of the glass on the top ($z = 0$) and bottom ($z = -500$ μm) surfaces. While in the central zone, the temperature difference ΔT remains almost constant at 47.7 K, there is a rapid decrease close to the sides, down to 24.5 K. Therefore, such temperature variations between the channels should be considered when calculating the mass flow rate and pressure difference in a pump with

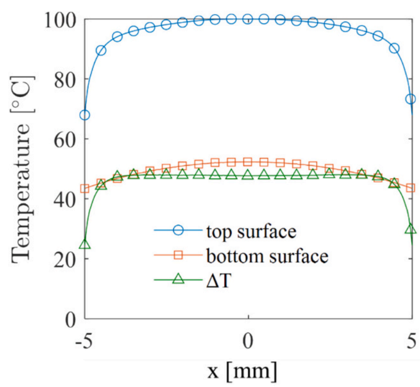

Fig. 9. Temperature profiles along the central line x of the glass plate for both top ($z = 0$) and bottom ($z = -500$ μm) surfaces, including their temperature difference ΔT.

multiple parallel channels. Section 6 presents the kinetic algorithm developed to investigate how variations in temperature differences affect the mass flow rate and pressure difference of the single-stage Knudsen pump design.

5. Fabrication process

Fabricating the proposed pump presents a significant challenge and requires careful consideration of available fabrication techniques. Bessel beam technology is a promising approach, as it enables the fabrication of high-aspect-ratio nanochannels with precise control over their geometry [51,52]. Since this method is well-suited for large-scale production of the nanochannels required for the Knudsen pump, it is applied in the present work. In addition, the complete device requires several advanced microfabrication steps beyond the nanochannel fabrication itself. Although each individual fabrication step is feasible and based on existing microfabrication technologies, the complete fabrication and integration of the full pump architecture are still ongoing. The complete fabrication process, illustrated in Fig. 10, relies on a five-mask process and the Bessel beam technology for opening the channels, with the individual steps outlined below:

a) Silicon micro-pillars via RIE: The fabrication of heat extraction micro-pillars begins with photolithography on the upper surface of the silicon wafer. A 2-μm thick AZ ECI 3012 photoresist is deposited by spin coating after prior coating with an anti-reflective coating (BARC). The resulting resin patterns protect the silicon during dry etching. This anisotropic silicon etching, aimed at producing pillars with a diameter of 7 μm and a height of 15 μm, is carried out by reactive ion etching (RIE). The process is performed in an Alcatel AMS 4200 Bati for approximately 3 min under the following conditions: a RF power of 90 W, a chamber pressure of 7.1 Pa, a gas flow rate of 700 sccm for SF_6/C_4F_8, and a substrate temperature of -5 °C. These parameters result in an average etch rate of 5 μm min^{-1}.
b) Large circular through-silicon openings via DRIE: A second photolithography is then performed on the underside of the silicon wafer to mask the through-holes during deep RIE (DRIE) etching. A 40 μm-thick AZ 40XT photoresist is used to withstand the prolonged DRIE etching of the 400 μm-thick silicon wafer. The circular openings in the resist have a diameter of 80 μm, corresponding to a standard aspect ratio (depth/diameter) of 5. The Bosch process is carried out in the same RIE AMS 4200 system using the same etching parameters. Approximately 90% of the wafer thickness is etched over 80 min at an etching rate of 5 μm min^{-1}, followed by a slower second etch at 2 μm min^{-1} for 20 min to fully open the holes.
c) Anodic glass/silicon bonding: An anodic bonding of the borosilicate glass wafer to the silicon wafer is performed under vacuum, with 600 V applied at 420 °C for 12 min in an ML WB04 wafer bonding system. The quality of the anodic bond is assessed using infrared (IR) imaging.
d) Alignment patterns on the glass wafer: A third photolithography step, followed by a 2 μm RIE etching on the top surface of the glass wafer, creates alignment patterns that allow precise positioning of the nanochannels and their corresponding thermal actuators (heaters) on these nanochannels.
e) Nanochannels opening on the glass wafer: Using Bessel beam technology, a network of 294,294 channels is created on the 4-in. borosilicate plate by laser ablation over a 1 × 1 cm^2 surface. Each channel has a diameter of 0.6 μm, a depth of 500 μm, with a spacing of 20 μm between adjacent channels, which prevents the formation of cracks in the glass during fabrication. The previously etched alignment markers on the surface allow for precise positioning of the channel array on the glass substrate with an accuracy of less than 2 μm, thus ensuring accurate alignment with the silicon pillars and subsequent metal layers.
f) Metal layers: The heating elements are fabricated by deposition of two successive metal layers, starting with cathodic thermal evaporation of a thin 20 nm titanium (Ti) layer, followed by a 300 nm gold (Au) layer. The reduced thickness of the Ti layer results in a sheet resistance approximately 400 times higher than that of the Ti/Au bilayer, rendering losses related to parasitic access resistances negligible. The thickness of the deposited metal layers is measured via cross-sectional imaging using a scanning electron microscope (SEM).
g) Micro-heaters: The gold layer is selectively wet-etched using a KI/I_2 solution to define the electrical current leads, following the fourth level of the photolithography mask. Next, the Ti layer is also selectively wet-etched in hydrofluoric acid, using the fifth photolithography mask to define the desired pattern for the heaters.

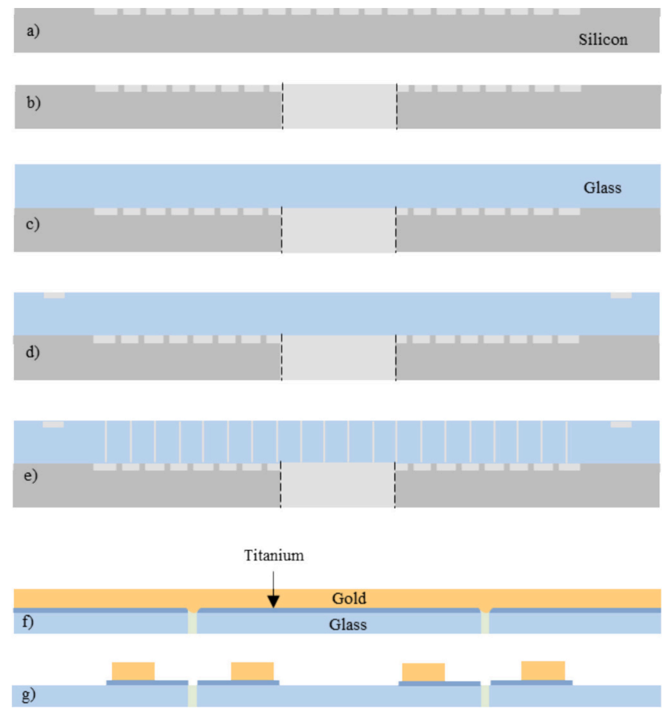

Fig. 10. Fabrication steps: a) RIE to form the silicon pillars, b) DRIE through the silicon wafer, c) anodic bonding of the glass to the silicon wafer, d) RIE of alignment patterns on the top surface of the glass, e) creation of channels using Bessel beams, f) deposition of metal layers, g) selective wet etching of gold and titanium. (For interpretation of the references to colour in this figure legend, the reader is referred to the web version of this article.)

The fabrication process presented above is intended to demonstrate the feasibility and integration of Bessel beam technology for the realization of nanochannels in atmospheric-pressure Knudsen pumps. The present study focuses on the overall pump design, thermal and gas flow analysis, and the proposed fabrication methodology. Detailed experimental characterization of the fabricated nanochannels, including fabrication tolerances, reproducibility, diameter variations, defect analysis, blockage probability, alignment accuracy, fabrication yield, and uncertainty quantification associated with the thermal and flow-performance, will be addressed in future work together with the experimental validation of the fabricated pump prototypes.

6. Performance study

In practice, it is quite challenging to maintain a constant temperature gradient along the lengths of several parallel channels and variations in the temperature gradient often occur (Fig. 8), which consequently affect the pressure difference and mass flow rate of the Knudsen pump. To simulate the mass flow rate and the pressure difference of such a pump, an iterative scheme has been developed and applied. The corresponding flowchart and its visual interpretation are presented in Figs. 11 and 12, respectively. Although the scheme described below is the same for linear and non-linear temperature distributions along the channels, for simplicity, a linear temperature distribution was assumed and thus, the different temperature gradients of the channels can be characterized by the temperature difference ΔT_i at the two ends of the channels, where subscript i denotes channel i. These temperature differences are known from the heat transfer simulations and fixed during the kinetic calculations. It is also noted that in the present model, the inlet and outlet pressures are assumed to be spatially uniform across all channels. This assumption is justified by the fact that the upstream and downstream reservoirs are significantly larger than the nanochannel dimensions, while the generated flow rates are small. Therefore, pressure non-uniformities and multidimensional flow interactions outside the channels are neglected.

The iterative scheme to find the pressure difference ΔP for a requested total mass flow $\dot{m}_{tot,req}$ reads as:

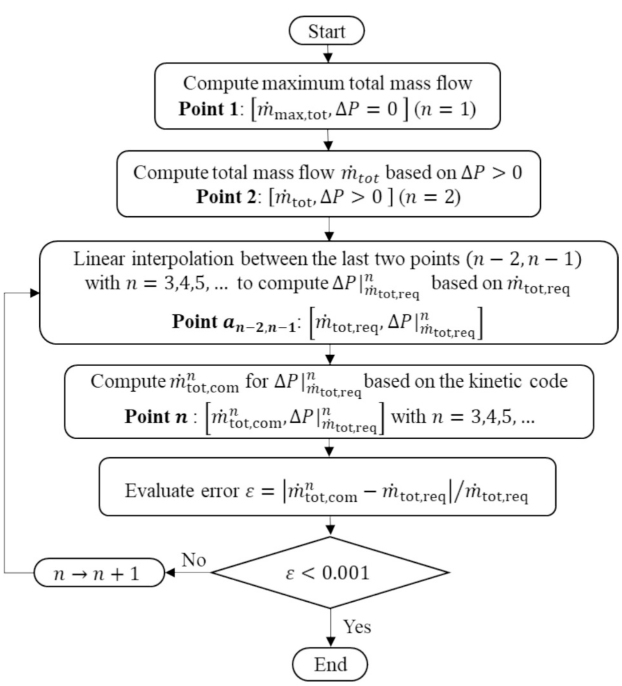

Fig. 11. Flowchart of the iterative scheme.

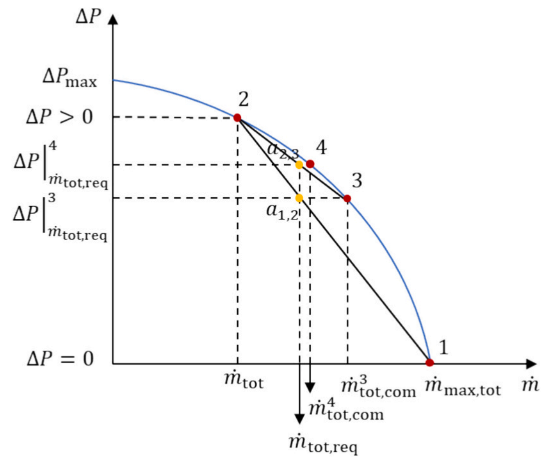

Fig. 12. Visual interpretation of the first four points ($n = 1, 2, 3, 4$).

- First, the total maximum mass flow $\dot{m}_{\max,tot}$ is computed by adding the maximum mass flow rates $\dot{m}_{\max,i}$ (for $\Delta P = 0$) of each channel

$$\dot{m}_{\max,tot} = \sum_{i=1}^{N} \dot{m}_{\max,i}(\Delta T_i) \tag{3}$$

to obtain Point 1 ($n = 1$): $[\dot{m}_{\max,tot}, \Delta P = 0]$.

- Next, the pressure difference ΔP between the two ends of the channels is set to a value greater than zero ($\Delta P > 0$). While, in practice, any ΔP greater than zero can be chosen, here, the maximum pressure difference $\Delta P_{\max}$ (for $\dot{m} = 0$) that can be achieved from the channel with the smaller ΔT is used. This choice provides a second point within the characteristic curve. In this case, the total mass flow rate $\dot{m}_{tot}$ is computed by adding the mass flow rates $\dot{m}_i$ of each channel

$$\dot{m}_{tot}(\Delta P) = \sum_{i=1}^{N} \dot{m}_i(\Delta P, \Delta T_i) \tag{4}$$

to obtain Point 2 ($n = 2$): $[\dot{m}_{tot}, \Delta P > 0]$.

- Having computed two points of the characteristic curve ($n = 1, 2$), the pressure difference $\Delta P|^{n}_{\dot{m}_{tot,req}}$ with $n = 3, 4, 5\ldots$ for a requested total mass flow $\dot{m}_{tot,req}$ can be approximated by linearly interpolating between these two points to obtain Point $a_{n-2,n-1}$: $\left[\dot{m}_{tot,req}, \Delta P|^{n}_{\dot{m}_{tot,req}}\right]$.
- Based on $\Delta P|^{n}_{\dot{m}_{tot,req}}$, the total mass flow rate computed from the kinetic code for each channel $\dot{m}^{n}_{tot,com} = \sum_{i=1}^{N} \dot{m}^{n}_{i,com}$ can be determined and the error can be evaluated as $\varepsilon = \left|\dot{m}^{n}_{tot,com} - \dot{m}_{tot,req}\right| / \dot{m}_{tot,req}$. If the error is small, the iterative scheme can be stopped. Otherwise, a new $\Delta P|^{n}_{\dot{m}_{tot,req}}$ by increasing n by 1 can be computed for $\dot{m}_{tot,req}$ through linear interpolation between the last two points ($n-2, n-1$). The iterations continue until convergence is achieved.

As a test case, the previously described iterative scheme is applied to a single-stage pump with four parallel channels subjected to different temperature differences: $\Delta T_1 = 80$ K, $\Delta T_2 = 70$ K, $\Delta T_3 = 60$ K, $\Delta T_4 = 50$ K, and $P_{in} = 1$ atm. For all channels, the hot temperature is set to 373 K, the channel radius is $r = 0.3\ \mu$m, the length is $l = 500\ \mu$m, and nitrogen gas is considered. The characteristic curves for each channel, denoted as c_1, c_2, c_3, and c_4, as well as for the entire pump operating with all four channels in parallel under two conditions—a) different ΔT_i with $i = 1, 2, 3, 4$ (c_5), and b) with the average temperature difference $\Delta T_m = 65$ K (c_6)—are plotted in Fig. 13.

It is observed that the maximum mass flow rate of the total system, $\dot{m}_{\max,tot}$, naturally equals the sum of the maximum mass flow rates of the

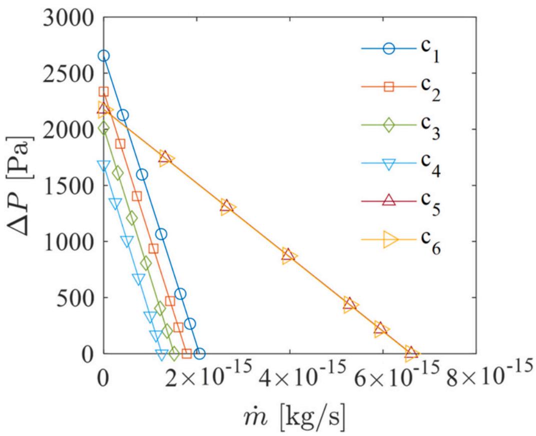

Fig. 13. Characteristic curves for each single channel subjected respectively to $\Delta T_1 = 80$ K, $\Delta T_2 = 70$ K, $\Delta T_3 = 60$ K, $\Delta T_4 = 50$ K (namely c_1, c_2, c_3, c_4) and for the entire pump with the four channels in parallel subjected to the different ΔT_i (c_5) or to the same mean $\Delta T_m = 65$ K (c_6).

individual channels, $\dot{m}_{\max,i}$, while the maximum pressure difference of the total system, $\Delta P_{\max,tot}$, equals the mean of the maximum pressure differences of the individual channels, $\Delta P_{\max,i}$. Although the latter statement is valid for the present case, it may not hold when the channels have different dimensions. In such cases, information about the geometry of each channel must be provided to the algorithm.

Moreover, the characteristic curves c_5 and c_6 are very close to each other, indicating that a system with varying ΔT across the channels can be approximated by a system in which all channels share the same average temperature difference ΔT_m. Furthermore, the characteristic curve of the four parallel channels remains linear, similar to that of single channels. As expected, both $\dot{m}_{\max}$ and $\Delta P_{\max}$ of a single channel decrease as the temperature difference ΔT decreases.

The iterative scheme is also applied to 200 channels uniformly distributed along the 1 cm-long central line of the glass plate by using a) the actual temperature difference ΔT distribution presented in Fig. 9 and b) the mean temperature difference $\Delta T_m = 46.6$ K while in both cases the inlet pressure is set to $P_{in} = 1$ atm. The resulting characteristic curves coincide each other indicating that the mean temperature assumption can also work in the case of 294,294 parallel channels of the proposed design. The mean temperature difference ΔT_m of the 294,294 channels design has been calculated by the ANSYS simulation and is equal to 46.8 K. Based on this ΔT_m, the characteristic curve is plotted in Fig. 14, showing a maximum mass flow rate $\dot{m}_{\max,tot} = 3.43 \times 10^{-10}$ kg s^{-1} and a maximum pressure difference $\Delta P_{\max} = 1575$ Pa, and a linear trend between the two endpoints.

To provide a quantitative comparison with previously reported Knudsen pumps, the mass flow rate per channel area and the pressure difference per stage are used as comparative performance metrics, as commonly adopted in the literature [35]. Using these metrics, the present design achieves a mass flow rate per channel area of 4.1×10^{-3} kg s^{-1} m^{-2}, which is about four orders of magnitude higher than the value previously reported in [35] (8.8×10^{-7} kg s^{-1} m^{-2}), while maintaining a pressure difference of 1575 Pa for a single stage, which is among the highest reported values for Knudsen pumps. The comparison was conducted based on the results summarized in [35], indicating the strong potential of the proposed architecture in pumping performance compared with previously reported Knudsen pumps.

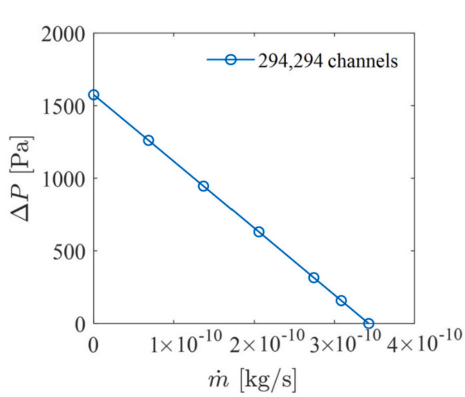

Fig. 14. Characteristic curve of the 294,294 parallel channels design.

To further increase the mass flow rate, additional channels should be introduced in parallel by both increasing the channel density and enlarging the active substrate area occupied by the channels. In the present design, the density of nanochannels can be further increased by reducing the spacing between adjacent channels from 20 to 10 μm, while the active area may be extended from the current 1 × 1 cm^2 configuration to larger wafer-scale substrates, such as standard 4-in. glass wafers. Furthermore, multiple pump stages can be vertically stacked with appropriate lateral electrical interconnections and thermal management solutions for heat removal. These approaches indicate that scaling the system is feasible from a fabrication and integration perspective. Nevertheless, the proposed design should be regarded as a first step toward the realization of a Knudsen pump operating under atmospheric conditions. Additional investigations are still required to improve both the achievable mass flow rate and pressure difference, as well as to address practical challenges related to large scale integration, fabrication tolerances, thermal management, and system level implementation.

To achieve stacking of multiple pump stages in series, the parallel microchannels of different stages are connected by macrochannels with significantly larger diameters than the microchannels. These macrochannels are used to separate the microchannels of sequential stages, creating regions where the high temperature at the end of one stage drops to the lower temperature at the beginning of the next one. This design minimizes the counterflow due to thermal creep in the macrochannels, ensuring that the thermal creep flow generated by the microchannels remains dominant.

To simulate a pump with multiple stages, the algorithm for a single stage with parallel channels has been extended to take also into account the counterflow in the macrochannels. More specifically, the pressure at the inlet of each macrochannel is set equal to the pressure at the outlet of the microchannels from the previous stage, while the pressure at the outlet of the macrochannel is set equal to the pressure at the inlet of the microchannels in the next stage. The flow in the macrochannels is computed by solving Eq. (1) as in the case of the microchannels but with a reversed temperature gradient. By defining the number of stages, specifying the geometry of both the microchannels and macrochannels, and setting the operating conditions, such as the initial pressure at the inlet of the first stage and the temperature gradient at each stage, the pressure difference of the multistage pump at zero mass flow rate can be determined. Subsequently, by incrementally increasing the mass flow rate through the pump, the characteristic curve can be drawn, and the maximum mass flow rate can be identified by finding the point where the pressure difference reaches zero. The process is similar to that described in [42,53], except that, at each stage, the algorithm which computes the mass flow and pressure differences among several parallel channels with different temperature distributions is applied.

With a complete gas flow simulation algorithm for a pump with multiple parallel channels and stages, along with realistic heat transfer data for operation up to 100 °C, it is possible to determine the number of channels and stages required to fulfill the specifications of a specific application, such as the one of the miniaturized pulsed tube cryocooler (PTCC) targeted by the PuCK project. In that case, a pump operating with a mean temperature difference of approximately $\Delta T_m = 50$ K and using channels with a radius $R = 0.3\,\mu$m would require 160 million parallel channels and 240 stages to achieve the requested mass flow rate of 10^{-7} kg s^{-1} and pressure difference of 1 bar. Although these requirements remain challenging and require further improvements in fabrication and system integration, the design proposed in this paper should be regarded as a first step toward the long-term goal of implementing Knudsen pumps in miniaturized PTCCs.

7. Concluding remarks

In the present work, a design and feasibility study of a single-stage Knudsen pump intended for operation at atmospheric and over-atmospheric pressures is presented, supported by heat transfer and gas flow simulations together with a proposed fabrication approach. The study has investigated the use of Bessel beam microfabrication for the realization of high-aspect-ratio nanochannels in glass with high writing speeds. The originality of the work lies primarily in applying this technology to Knudsen pump fabrication, while well-established thermal and kinetic modeling approaches were used to optimize the pump design and predict its performance. To the authors' knowledge, this is the first proposed application of Bessel beam technology to Knudsen pumps, extending current manufacturing possibilities for submicron-channel devices. Fabrication and experimental testing of the proposed pump architecture will be the subject of future work.

In contrast to DRIE, which is a widely used technique for fabricating micrometer-scale structures, Bessel beam technology can produce submicron channels with high aspect ratios and very high repetition rates. As such, it offers a promising alternative for the fabrication of Knudsen pumps designed to operate at or above atmospheric pressure. Taking into account the current limitations of this technology, a single-stage Knudsen pump design has been proposed. A 4-in., 500 μm-thick glass wafer was divided into nine 2×2 cm^2 sections, each serving as an individual pump. The central 1×1 cm^2 region of each pump contains 600 nm-diameter nanochannels arranged in a hexagonal pattern, for a total of 294,294 channels. Thin-film heaters, consisting of titanium and gold layers, were deposited on the top surface to localize heating around the channels. On the bottom side, a 500 μm-thick silicon wafer with 15 μm-high and 7 μm-diameter pillars—offset from the channels—acts as a heat sink to remove the generated heat. In addition, 80 μm-diameter openings etched through the silicon wafer allow the gas to flow from the underside.

To determine the optimal channel radius, results obtained from the thermal transpiration flow through single channels were used. For operation at atmospheric pressure, a radius of 0.3 μm was found to yield the maximum pressure difference. For this same diameter, the resulting mass flow rate remains significant and close to the plateau reached for larger radii.

Heat transfer simulations of the Knudsen pump were performed in ANSYS to optimize the design based on the temperature gradient along the glass thickness and, consequently, across the nanochannels. It was found that a simple configuration without a bottom heat sink leads to low performances. Therefore, a more advanced design was proposed, incorporating heaters around each channel on the top side of the glass and silicon pillars surrounding each channel on the bottom side. This configuration significantly improves both the temperature gradient and the number of channels over which it can be effectively applied. When 10 W of power is applied to heat the top surface of the glass plate, a mean temperature difference of 46.8 K is predicted across the 294,294 nanochannels.

For the fabrication of the pump, a series of advanced microfabrication techniques is planned. First, RIE is used to create silicon pillars on the top surface of a silicon wafer, followed by DRIE to open large through-holes across its entire thickness. The silicon wafer is then anodically bonded to the bottom side of the glass wafer. Using the Bessel beams technology, 294,294 nanochannels are formed in the glass, after which two metallic layers of titanium and gold are deposited and selectively etched to define the heaters and their electrical interconnections.

To accurately simulate the gas flow in the proposed design, the kinetic algorithm for a single channel was extended to account for multiple parallel channels with different temperature gradients. It was found that assuming the mean temperature gradient across the channels yields accurate results for the present study. Based on the simulations, the proposed design can provide a maximum mass flow rate $\dot{m}_{\max,tot} = 3.43 \times 10^{-10}$ kg s^{-1} and a maximum pressure difference $\Delta P_{\max} = 1575$ Pa. When normalized by the total channel area, the predicted mass flow rate is much higher than that of previously reported Knudsen pumps, while maintaining a pressure difference among the highest values reported in the literature. While these simulation results indicate that further optimization is required to reach application-level performance, they demonstrate the feasibility and potential of the proposed architecture for the development of Knudsen pumps operating at atmospheric and higher pressures. The kinetic algorithm has also been extended to multiple stages and can been used to estimate the number of parallel channels and stages required to achieve the desired mass flow rate and pressure difference.

Although the results demonstrate the potential of Bessel beam microfabrication for atmospheric-pressure Knudsen pumps, several limitations remain in the present study. The reported performances are based on numerical simulations and have not yet been experimentally validated. In addition, the proposed fabrication methodology still requires detailed characterization in terms of fabrication tolerances, reproducibility, channel diameter variations, defect formation, blockage probability, alignment accuracy, fabrication yield and uncertainty quantification associated with the thermal and flow-performance. Further optimization is also needed to increase the achievable mass flow rate and pressure difference, as well as to address challenges related to large-scale integration, thermal management, and multistage implementation. Future work will therefore focus on fabrication characterization, experimental validation, and further investigation of the scalability of the proposed pump architecture.

CRediT authorship contribution statement

Thanasis Basdanis: Writing – review & editing, Writing – original draft, Methodology, Investigation, Formal analysis, Conceptualization. **Phassawat Leelaburanathanakul:** Writing – review & editing, Investigation. **Thierry Camps:** Writing – review & editing, Validation, Supervision, Resources, Methodology, Conceptualization. **Marcos Rojas-Cárdenas:** Writing – review & editing, Validation, Supervision, Methodology, Investigation, Formal analysis, Conceptualization. **Christine Barrot:** Writing – review & editing, Validation, Supervision, Methodology, Conceptualization. **Lucien Baldas:** Writing – review & editing, Validation, Supervision, Project administration, Methodology, Investigation, Funding acquisition, Conceptualization. **Jürgen J. Brandner:** Writing – review & editing, Validation, Supervision, Project administration, Methodology, Funding acquisition, Conceptualization. **Stéphane Colin:** Writing – review & editing, Validation, Supervision, Methodology, Formal analysis, Conceptualization.

Declaration of competing interest

The authors declare the following financial interests/personal relationships which may be considered as potential competing interests:

Acknowledgments

This work was funded by the French National Research Agency (ANR) and the German Research Agency (DFG) under the project "ANR-2022-CE92-0017-01" and "DFG BR 4175/8-1". This work was supported by LAAS-CNRs micro and nanotechnologies platform, a member of the Renatech French national network. The authors would like to thank the

FEMTO-ST team in Besançon, in particular Francois Courvoisier and Jassem Safioui, concerning the creation of nanochannels using Bessel beam technology. Special thanks are also extended to Adrian Laborde for his support with the photolithography processes and to Aurélie Lecestre and Mathieu Arribat for their contribution to the DRIE fabrication. The authors also gratefully acknowledge Franz Schweizer for the insightful discussions regarding the simulations and fabrication processes of the pump.

Data availability

Data will be made available on request.

References

[1] X. Wang, T. Su, W. Zhang, Z. Zhang, S. Zhang, Knudsen pumps: a review, Microsyst. Nanoeng. 6 (2020) 26.
[2] T. Grzebyk, MEMS vacuum pumps, J. Microelectromech. Syst. 26 (2017) 705–717.
[3] A. Górecka-Drzazga, Miniature and MEMS-type vacuum sensors and pumps, Vacuum 83 (2009) 1419–1426.
[4] S. McNamara, Y.B. Gianchandani, On-chip vacuum generated by a micromachined Knudsen pump, J. Microelectromech. Syst. 14 (2005) 741–746.
[5] Q. Xiao, D. Zeng, Z. Yu, S. Zou, Z. Liu, Study on rapid prediction of flow field in a Knudsen compressor based on multi-fidelity reduced-order models, Int. J. Hydrog. Energy 86 (2024) 519–529.
[6] Y. Huang, J. Ye, D. Li, J. Xie, X. He, Numerical investigation of flow and transmission behaviors in multi-stage hydrogen Knudsen pump with blocked microchannel, Appl. Therm. Eng. 280 (2025) 128483.
[7] Y. Qin, Y.B. Gianchandani, A fully electronic microfabricated gas chromatograph with complementary capacitive detectors for indoor pollutants, Microsyst. Nanoeng. 2 (2016) 15049.
[8] Q. Cheng, Y. Qin, Y.B. Gianchandani, A bidirectional Knudsen pump with superior thermal management for micro-gas chromatography applications, 2017 IEEE 30th International Conference on Micro Electro Mechanical Systems (MEMS), 2017, pp. 167–170.
[9] T. Byambadorj, Q. Cheng, Y. Qin, Y.B. Gianchandani, A monolithic Si-micromachined four-stage Knudsen pump for μGC applications, J. Micromech. Microeng. 31 (2021) 034001.
[10] Y.-B. Zhao, T. Wu, C. Heimhofer, N. Heppeler, M. Gao, T. Cen, F. Weyand, C. Ludwig, S. Zhao, J. Wang, An aerogel-based light-driven Knudsen pump approaching complete passive capturing of airborne particles in wide size ranges, Fundam. Res. (2025).
[11] A. Ajuda, G. Silva, V. Semiao, Performance analysis of multi-capillary Knudsen heat pumps, Fluids 10 (2025) 236.
[12] K. Kugimoto, Y. Hirota, T. Yamauchi, H. Yamaguchi, T. Niimi, Design and demonstration of Knudsen heat pump without moving parts free from electricity, Appl. Energy 250 (2019) 1260–1269.
[13] K. Kugimoto, Y. Hirota, T. Yamauchi, H. Yamaguchi, T. Niimi, A novel heat pump system using a multi-stage Knudsen compressor, Int. J. Heat Mass Transf. 127 (2018) 84–91.
[14] S.E. Vargo, E.P. Muntz, W.C. Tang, The MEMS Knudsen Compressor as a Vacuum Pump for Space Exploration Applications, 2000.
[15] K. Hamasaki, R. Yano, K. Suzuki, Numerical study on application of Knudsen pump to thruster of spacecraft, Trans. Jpn. Soc. Aeronaut. Space Sci. Aerospace Technol. Jpn. 10 (2012) Pe_73-Pe_80.
[16] F. Ejeian, S. Azadi, A. Razmjou, Y. Orooji, A. Kottapalli, M. Ebrahimi Warkiani, M. Asadnia, Design and applications of MEMS flow sensors: A review, Sensors Actuators A Phys. 295 (2019) 483–502.
[17] A. Bell, W.D. Ehringer, S. McNamara, Scavenged body heat powered infusion pump, J. Micromech. Microeng. 23 (2013) 114019.
[18] R. Radebaugh, Cryocoolers: the state of the art and recent developments, J. Phys. Condens. Matter 21 (2009) 164219.
[19] R. Lewis, Y. Wang, J. Cooper, M. Lin, V. Bright, Y. Lee, P. Bradley, R. Radebaugh, M. Huber, Micro cryogenic coolers for IR imaging, in: Proceedings of SPIE - the International Society for Opt. Eng., 8012, 2011.
[20] N. Almtireen, J.J. Brandner, J.G. Korvink, Pulse tube cryocooler: Phasor analysis and one-dimensional numerical simulation, J. Low Temp. Phys. 199 (2020) 1179–1197.
[21] M. Knudsen, Thermischer Molekulardruck der Gase in Röhren, Ann. Phys. 338 (1910) 1435–1448.
[22] M. Knudsen, Eine Revision der Gleichgewichtsbedingung der Gase. Thermische Molekularströmung, Ann. Phys. 336 (1909) 205–229.
[23] O. Reynolds, XVIII. On certain dimensional properties of matter in the gaseous state. - Part I. Experimental researches on thermal transpiration of gases through porous plates and on the laws of transpiration and impulsion, including an experimental proof that gas is not a continuous plenum. - Part II. On an extension of the dynamical theory of gas, which includes the stresses, tangential and normal, caused by a varying condition of gas, and affords an explanation of the phenomena of transpiration and impulsion, Philos. Trans. R. Soc. Lond. (1879) 727–845.
[24] J.C. Maxwell, VII. On stresses in rarified gases arising from inequalities of temperature, Philos. Trans. R. Soc. Lond. (1879) 231–256.
[25] Y. Sone, Molecular Gas Dynamics: Theory, Techniques, and Applications, Birkhäuser, Boston, 2007.
[26] F. Sharipov, V. Seleznev, Data on internal rarefied gas flows, J. Phys. Chem. Ref. Data Monogr. 27 (1998) 657–706.
[27] T. Ohwada, Y. Sone, K. Aoki, Numerical analysis of the shear and thermal creep flows of a rarefied gas over a plane wall on the basis of the linearized Boltzmann equation for hard-sphere molecules, Phys. Fluids A 1 (1989) 1588–1599.
[28] K. Ritos, Y. Lihnaropoulos, S. Naris, D. Valougeorgis, Pressure- and temperature-driven flow through triangular and trapezoidal microchannels, Heat Transfer Eng. 32 (2011) 1101–1107.
[29] T. Basdanis, G. Tatsios, D. Valougeorgis, Gas-surface interaction in rarefied gas flows through long capillaries via the linearized Boltzmann equation with various boundary conditions, Vacuum 202 (2022) 111152.
[30] P. Wang, W. Su, L. Wu, Thermal transpiration in molecular gas, Phys. Fluids 32 (2020) 082005.
[31] M. Rojas-Cárdenas, I. Graur, P. Perrier, J.G. Méolans, Thermal transpiration flow: A circular cross-section microtube submitted to a temperature gradient, Phys. Fluids 23 (2011) 031702.
[32] H. Yamaguchi, M. Rojas-Cárdenas, P. Perrier, I. Graur, T. Niimi, Thermal transpiration flow through a single rectangular channel, J. Fluid Mech. 744 (2014) 169–182.
[33] M. Rojas-Cárdenas, I. Graur, P. Perrier, J.G. Méolans, A new method to measure the thermal slip coefficient, Int. J. Heat Mass Transf. 88 (2015) 766–774.
[34] H. Yamaguchi, P. Perrier, M.T. Ho, J.G. Méolans, T. Niimi, I. Graur, Mass flow rate measurement of thermal creep flow from transitional to slip flow regime, J. Fluid Mech. 795 (2016) 690–707.
[35] T. Byambadorj, X. Zhao, Y. Qin, Y.B. Gianchandani, Monolithic SOI through-wafer Knudsen pumps with mechanically robust Si channels, Sensors Actuators A Phys. 365 (2024) 114825.
[36] N.V. Toan, N. Inomata, N.H. Trung, T. Ono, Knudsen pump produced via silicon deep RIE, thermal oxidation, and anodic bonding processes for on-chip vacuum pumping, J. Micromech. Microeng. 28 (2018) 055001.
[37] N.K. Gupta, Y.B. Gianchandani, Thermal transpiration in mixed cellulose ester membranes: Enabling miniature, motionless gas pumps, Microporous Mesoporous Mater. 142 (2011) 535–541.
[38] N.K. Gupta, Y.B. Gianchandani, Porous ceramics for multistage Knudsen micropumps - modeling approach and experimental evaluation, J. Micromech. Microeng. 21 (2011) 095029.
[39] A. Faiz, S. McNamara, A.D. Bell, G. Sumanasekera, Nanoporous Bi2Te3 thermoelectric based Knudsen gas pump, J. Micromech. Microeng. 24 (2014) 035002.
[40] V. Kosyanchuk, A. Petrov, M. Kik, M. Yagodina, R. Seredenko, Theoretical and experimental study of 3D-printed Knudsen pump with liquid cooling, Int. J. Heat Mass Transf. 249 (2025) 127178.
[41] S. An, Y. Qin, Y.B. Gianchandani, A monolithic high-flow Knudsen pump using vertical Al2O3 channels in SOI, J. Microelectromech. Syst. 24 (2015) 1606–1615.
[42] G. López Quesada, G. Tatsios, D. Valougeorgis, M. Rojas-Cárdenas, L. Baldas, C. Barrot, S. Colin, Thermally driven pumps and diodes in multistage assemblies consisting of microchannels with converging, diverging and uniform rectangular cross sections, Microfluid. Nanofluid. 24 (2020) 54.
[43] G. Tatsios, G. Lopez Quesada, M. Rojas-Cardenas, L. Baldas, S. Colin, D. Valougeorgis, Computational investigation and parametrization of the pumping effect in temperature-driven flows through long tapered channels, Microfluid. Nanofluid. 21 (2017) 99–91:17.
[44] S. An, N.K. Gupta, Y.B. Gianchandani, A Si-micromachined 162-stage two-part Knudsen pump for on-chip vacuum, J. Microelectromech. Syst. 23 (2014) 406–416.
[45] F. Schweizer, K. Bade, L. Baldas, S. Bergdolt, S. Colin, C. Deutschbein, S. Hengsbach, J.G. Korvink, M. Rojas-Cárdenas, J.J. Brandner, Rarefied gas flows in complex microfluidic 3D-structures fabricated via additive manufacturing, Vacuum 238 (2025) 114213.
[46] N. Gaignebet, M. Rojas-Cárdenas, S. Colin, S. Raffy, M. Raison, É. Palleau, Cost and time-efficient micro-device fabrication process for rarefied gas flows applications, Phys. Fluids 36 (2024) 121707.
[47] D. Zhang, G. López-Quesada, S. Bergdolt, S. Hengsbach, K. Bade, S. Colin, M. Rojas-Cárdenas, 3D micro-structures for rarefied gas flow applications manufactured via two-photon-polymerization, Vacuum 211 (2023) 111915.
[48] R. Brancher, M.V. Johansson, P. Perrier, I. Graur, Measurements of pressure gradient and temperature gradient driven flows in a rectangular channel, J. Fluid Mech. 923 (2021) A35.
[49] K. Srinivasan, P.M.V. Subbarao, S.R. Kale, Studies on gas flow through smooth microchannel surface – fabrication, characterization, analysis, and tangential momentum accommodation coefficient comparison, Heat Transfer Eng. 41 (2020) 607–621.
[50] S. Kanehira, J. Si, J. Qiu, K. Fujita, K. Hirao, Periodic nanovoid structures via femtosecond laser irradiation, Nano Lett. 5 (2005) 1591–1595.
[51] L. Rapp, R. Meyer, R. Giust, L. Furfaro, M. Jacquot, P.A. Lacourt, J.M. Dudley, F. Courvoisier, High aspect ratio micro-explosions in the bulk of sapphire generated by femtosecond Bessel beams, Sci. Rep. 6 (2016) 34286.
[52] R. Meyer, L. Froehly, R. Giust, J. Del Hoyo, L. Furfaro, C. Billet, F. Courvoisier, Extremely high-aspect-ratio ultrafast Bessel beam generation and stealth dicing of multi-millimeter thick glass, Appl. Phys. Lett. 114 (2019) 201105.
[53] G. López Quesada, G. Tatsios, D. Valougeorgis, M. Rojas-Cárdenas, L. Baldas, C. Barrot, S. Colin, Design guidelines for thermally driven micropumps of different architectures based on target applications via kinetic modeling and simulations, Micromachines 10 (2019) 249.

[54] F. Sharipov, Rarefied gas flow through a long tube at any temperature ratio, J. Vac. Sci. Technol. A 14 (1996) 2627–2635.
[55] G. Tatsios, D. Valougeorgis, Uncertainty analysis of computed flow rates and pressure differences in rarefied pressure and temperature driven gas flows through long capillaries, Eur. J. Mech. B. Fluids 79 (2020) 190–201.
[56] T. Basdanis, G. Tatsios, D. Valougeorgis, Sensitivity analysis of the Cercignani - Lampis accommodation coefficients in prototype rarefied gas flow and heat transfer problems via the Monte Carlo method, Eur. J. Mech. B. Fluids 107 (2024) 80–94.
[57] M. Rojas-Cardenas, I. Graur, P. Perrier, J.G. Meolans, Time-dependent experimental analysis of a thermal transpiration rarefied gas flow, Phys. Fluids 25 (2013) 072001.
[58] C. Tantos, Polyatomic thermal creep flows through long microchannels at large temperature ratios, J. Vac. Sci. Technol. A 37 (2019).
[59] L. Wu, H. Struchtrup, Assessment and development of the gas kinetic boundary condition for the Boltzmann equation, J. Fluid Mech. 823 (2017) 511–537.
[60] A.A. Abdeslam, K. Fouas, A. Khalifa, Design and optimization of platinum heaters for gas sensor applications, Dig. J. Nanomater. Biostruct. 15 (2020) 133–141.
[61] S. Singh, A. Jejusaria, J. Singh, M. Vashishath, D. Kumar, Comparative study of titanium, platinum, and titanium nitride thin films for micro-elecrto mechanical systems (MEMS) based micro-heaters, AIP Adv. 12 (2022).
[62] K.L. Zhang, S.K. Chou, S.S. Ang, Fabrication, modeling and testing of a thin film au/Ti microheater, Int. J. Therm. Sci. 46 (2007) 580–588.
[63] P. Dixit, N. Lin, J. Miao, W.K. Wong, T.K. Choon, Silicon nanopillars based 3D stacked microchannel heat sinks concept for enhanced heat dissipation applications in MEMS packaging, Sensors Actuators A Phys. 141 (2008) 685–694.
[64] L. Zhang, K.E. Goodson, T.W. Kenny, Silicon Microchannel Heat Sinks: Theories and Phenomena, Springer, Berlin, 2004.
[65] Z.-Q. Yu, M.-T. Li, B.-Y. Cao, A comprehensive review on microchannel heat sinks for electronics cooling, Int. J. Extreme Manuf. 6 (2024) 022005.
[66] K. Lu, C. Wang, C. Wang, X. Fan, F. Qi, H. He, Topological structures for microchannel heat sink applications – a review, Manuf. Rev. 10 (2023) 2.
[67] A. Joy, S.K. V, B. Baby, Review on fabrication and experimental study of microchannel heat sinks for cooling of electronic components, Mater. Today Proc. 72 (2023) 2985–2991.
[68] N. Cassada, C. Anderson, L. Kubicek, D. Hobby, C. Frye, S. Baxamusa, J. Kotovsky, K. Jackson, I. Ladner, T. Bandhauer, SiC microchannel heat sinks for high heat flux dissipation of 1 kW/cm2, IEEE Trans. Compon. Packag. Manuf. Technol. 13 (2023) 655–665.
[69] D. Jung, H. Lee, D. Kong, E. Cho, K.W. Jung, C.R. Kharangate, M. Iyengar, C. Malone, M. Asheghi, K.E. Goodson, H. Lee, Thermal design and management of micro-pin fin heat sinks for energy-efficient three-dimensional stacked integrated circuits, Int. J. Heat Mass Transf. 175 (2021) 121192.
[70] D. Kesavan, R. Senthil Kumar, P. Marimuthu, Heat transfer performance of air-cooled pin–fin heatsinks: a review, J. Therm. Anal. Calorim. 148 (2023) 623–649.
[71] P. Bhandari, K.S. Rawat, Y.K. Prajapati, D. Padalia, L. Ranakoti, T. Singh, Design modifications in micro pin fin configuration of microchannel heat sink for single phase liquid flow: A review, J. Energy Storage 66 (2023) 107548.
[72] Y. Li, L. Gong, M. Xu, Y. Joshi, Thermal performance analysis of biporous metal foam heat sink, J. Heat Transf. 139 (2017).
[73] S.A.B. Al-Omari, Z.A. Qureshi, E. Elnajjar, F. Mahmoud, A heat sink integrating fins within high thermal conductivity phase change material to cool high heat-flux heat sources, Int. J. Therm. Sci. 172 (2022) 107190.